www.sciencemag.org/content/345/6194/298/suppl/DC1

Supplementary Materials for

Dielectric gradient metasurface optical elements

Dianmin Lin, Pengyu Fan, Erez Hasman, Mark L. Brongersma*

*Corresponding author. E-mail: brongersma@stanford.edu

Published 18 July 2014, *Science* **345**, 298 (2014)
DOI: 10.1126/science.1253213

This PDF file includes:

Materials and Methods
Figs. S1 to S10
Legends for Movies S1 to S3
Full Reference List

Other Supplementary Material for this manuscript includes the following:
(available at www.sciencemag.org/content/345/6194/298/suppl/DC1)
Movies S1 to S3

Materials and Methods

S1. Fabrication of DGMOEs

The fabrication process of DGMOEs begins with the deposition of a 100-nm-thick intrinsic poly-silicon film onto a quartz substrate using low-pressure chemical vapor deposition (LPCVD) at 620 °C. The complex refractive index of the poly-silicon film is characterized by a Spectroscopic Ellipsometer (Woollam, M2000) and is shown in Fig. S1A. The associated intrinsic absorption properties of the material are shown in Fig. S1B. Electron beam lithography and standard reactive-ion etching (HBr/Cl_2) techniques were employed to pattern the DGMOE patterns into the Si film.

S2. Optical setup for measuring the light intensity distributions produced by DGMOEs

The intensity distribution of the light transmitted through the metasurface is measured using a confocal microscope (Nikon Eclipse, C1). A schematic of the optical train is depicted in Fig. S2. The illumination source is a white light supercontinuum source that is wavelength-tunable from 400 to 2200 nm (NKT, SuperK Extreme). A linear polarizer and a quarter waveplate are utilized to generate a circularly polarized illumination beam. The samples with DGMOEs are mounted on an XYZ scan stage with the metasurface facing upwards towards the microscope objective. The laser beam is vertically illuminated onto the sample from substrate side. Images of the field intensity distribution at different heights above the DGMOE are confocally collected using a 100X objective with a numerical aperture (NA) of 0.9 and captured by a high-resolution CCD camera (Princeton Instruments, PIXIS 1024B). By controlling the distance between the sample stage and the objective, intensity distributions at the different planes above the sample can be imaged. Starting with the plane in which the metasurface is located, we took images at every 0.2 μm above the metasurface. With these images, we reconstructed the 3D light-intensity-profile of the transmitted light beam behind the metasurface.

S3. Phase delay in light scattering of TE and TM polarized light by a single Si nanobeam

Dielectric optical antennas based on silicon nanobeams support leaky mode resonances (*12*, *21*), which can effectively confine light within these subwavelength, high-refractive-index nanostructures. It has already been convincingly shown that single nanowire can support a series of Mie resonances under illumination with transverse electric (TE) or transverse magnetic (TM) polarized light (*15*). Some of the TE and TM resonances are degenerate and others occur at distinct frequencies. One can capitalize on these resonances to elicit a substantial phase retardation in the scattered light waves produced under TE and TM illumination. An example of this is shown in Figure S3, where a 120-nm-wide and 100-nm-high Si nanobeam is illuminated with either TE or TM polarized light. The resonant response of the single Si nanobeam that leads to energy storage in the nanobeams is reflected in the absorption efficiency spectra that shows a peak near the wavelength of 630 nm (see Fig. S3B). At a wavelength of 550 nm, just above the resonance, a substantial phase difference between TE and TM scattered waves can be observed (see Fig. S3C). When such nanobeams are used in arrays, the resonant response of these individual building blocks is reflected in the array and gives rise to a very strong birefringence.

S4. Experimental setup for quantifying the optical properties of Si nanobeam waveplates

The optical properties of the nanobeam waveplates, including the transmission coefficient t_{TE} and t_{TM} for TE and TM polarization respectively, and a phase retardation ϕ of TM polarized light with respect to TE polarized light, are characterized by a custom-built optical system. A schematic of the experimental setup is depicted schematically in Fig. S4.

The light source used in the experiments is a white light supercontinuum source that is tunable from 400 to 2200 nm (NKT, SuperK Extreme). A linear polarizer is utilized to produce a linearly polarized illumination beam with a polarization angle of 45 degrees with respect to the x- and y-axes. In this case, the incident wave has horizontal and vertical components of equal amplitude (E_0) and phase (φ_{TM}, φ_{TE}). A 20X objective is used to gently focus the incident light beam onto the nanobeam sample with a spot size of approximately 20 µm. The sample is mounted on an XYZ translation stage, with the nanobeams oriented along the vertical y-axis. A custom-built imaging system including another 20X objective and a tube lens was constructed to collect the transmitted light. A CCD camera on the transmission side was used to ensure that incident light beam was properly illuminating the area patterned with nanobeams. A quarter waveplate (QWP) and a linear polarizer (LP) were used to assess the state of polarization of the transmitted light.

As the light passes through the Si nanobeam waveplate, the polarization state of the light is altered and the horizontal component of the electric field is given by $E_{TE} = E_0 t_{TE} e^{-i\varphi_{TE}}$ for TE polarization, and vertical is component is similarly given by: $E_{TM} = E_0 t_{TM} e^{-i\varphi_{TM}}$. The polarization state of transmitted beam can be experimentally characterized by the four Stokes parameters I, Q, U, V. Therefore, from the Stokes parameters, we can obtain the optical properties of the transmission coefficient t_{TE} and t_{TM}, and the phase retardation $\phi = \varphi_{TM} - \varphi_{TE}$ between TM and TE polarized light. For Si nanobeam waveplate which has the fast axes perpendicular to the nanobeams, transmission coefficient t_{TE} and t_{TM}, are corresponding to t_x and t_y respectively in Eq.1 of the main text.

The Stokes parameters I, Q, U, V can be determined by means of four consecutive intensity measurements with different orientations of the QWP and LP using a well-established protocol that can be found in literature (*12*). In our setup, the transmission intensity was measured using a high resolution, calibrated CCD camera (Princeton Instruments, PIXIS 1024B).

S5. Spectrally-dependent optical properties of the Si nanobeam waveplates

We performed finite element simulations to predict the optical properties of the fabricated nanobeam waveplates consisting of a periodic array of Si nanobeams. Here, the nanobeams had a width of 120 nm, a thickness of 100 nm, and were spaced by 200 nm. To simulate the behavior, we used the optical properties of poly-Si that were measured by ellipsometry and presented in supplementary section S1. Figures S5A-C show the simulated spectral-dependence of the absorption, the transmission coefficient, and the phase delay of transmitted light for both TE (green) and TM (blue) polarized illumination.

The absorption spectrum plotted in Fig. S5A shows a pronounced peak for TE polarization near 600 nm. At this wavelength, the beams in the waveplate support a fundamental resonance with one antinode in the field distribution inside the nanobeam (See field distribution in the inset to

Fig.2D in the main text). In contrast, the absorption spectrum for TM polarized light does not show a pronounced resonant peak. It more-or-less follows the spectral dependence of the intrinsic materials absorption of poly-Si, as presented in Fig. S1B. Slight deviations in the spectral properties can be attributed to the excitation of a very weak second-order resonance with two antinodes in the body of the nanobeam.

Figure S5B plots the spectral dependence of the transmission coefficient. It features a dip in the spectrum near the TE resonance, where the electric field intensity in the absorbing nanobeams is high. It is worth pointing out that the two polarizations exhibit a more-or-less equal transmission at wavelengths close to 500 nm and 700 nm. This is desired to realize high diffraction efficiency DGMOEs as per Eq.1 in the main text.

Figure S5C shows the simulated spectra of the phase delay of the transmitted light under TE (green) and TM (blue) illumination with respect to a reference case in which a plane wave illuminates a sample without nanobeams. The results from both full-field electromagnetic simulations (continuous line) and an approximate zeroth-order effective medium theory (dashed line) are shown. In the zeroth-order effective medium theory, the dielectric constants for transverse-electric TE illumination (with the electric field polarized normal to the length of the nanobeams) and transverse-magnetic TM illumination (with the electric field along the length of the nanobeams) were calculated using the following two expressions (*27*):

$$\varepsilon_{TE} = \frac{\varepsilon_{Si}\varepsilon_{Air}}{f_{Si}\varepsilon_{Si} + f_{Air}\varepsilon_{Air}} \qquad \text{(Eq. S1)}$$

$$\varepsilon_{TM} = f_{Si}\varepsilon_{Si} + f_{Air}\varepsilon_{Air} \qquad \text{(Eq. S2)}$$

This zeroth-order approximation can accurately predict the behavior of a nanobeam array in the limit that the period is deep subwavelength ($P \ll \lambda$) and the normalized thickness $t/\lambda \gg 1$. In that limit, high diffraction-orders are evanescent and decay. For this reason, only the zeroth-order can propagate and is relevant to the optical properties of the array. The zeroth-order theory makes for an interesting reference case as it does not capture the effect of optical resonances in redistribution the fields from an incident wave to resemble the field distribution of the resonant modes supported by the nanobeams. In other words, the effect of optical resonances are not captured and a comparison to the full-field simulations (which do capture the impact of resonances) enable one to study the impact resonances have on the spectral dependence of the effective dielectric constants.

In the long wavelength limit ($\lambda > 800$ nm), the full-field simulations and effective medium theory both predict a phase delay for TE and TM polarized light that slowly increases with decreasing wavelength (See Fig. S5D). In this limit the zeroth-order effective medium theory is quite useful to capture the qualitative trend in the phase delay with decreasing wavelength. The increase is a trivial decrease due to the fact that the phase delay scales with the ratio of the nanobeam layer thickness and the wavelength (d/λ). Near the TE resonance, the phase delay for the TM light keeps on increasing with decreasing wavelength. For this polarization, the full-field simulation and the effective medium theory again predict qualitatively similar behavior. A different behavior is observed for TE polarized illumination. Whereas the zeroth-order effective medium theory predicts a monotonic increase in phase delay with decreasing wavelength, the full-field simulations show the impact of the TE resonance on the phase delay. This can be understood by viewing the beam array as a uniaxial crystal with effective optical properties. This type of (higher order) effective medium description is not just of value in the extreme case where the period is deep subwavelength ($P << \lambda$) and the normalized thickness $t/\lambda >> 1$ (i.e. where the zeroth-order effective medium approximation in Eqs S1 and S2 hold). It can still be of practical use for a broader set of situations for which $P/\lambda < 1/\{\max(n_1, n_2) + n_1 \sin(\psi)\}$ where n_1 and n_2 are the indices of the super and substrates for the array and ψ the incident angle of an incoming beam of light. In that case only zeroth transmitted and reflected orders can propagate. For our DGMOE patterned on a quartz substrate (n =1.45) and taking $\psi = \pi/2$ to allow for any desired angle of incidence, this implies that $P/\lambda < 1/2.45 \approx 0.41$. This condition allows for the beams to be sufficiently large to support strong optical resonances that can be built into the effective optical properties of the array. When the optical properties of a uniaxial crystal feature a resonance for one of the polarizations, the associated index will increase with increasing frequency on either side of the resonance (normal dispersion) and decrease in the immediate vicinity of the resonance (anomalous dispersion), as seen in the solid green curve in Fig. S5D around 600 nm. Overall, there is a decrease in the index with increasing frequency when moving spectrally across the resonance. In our case, the strong TE resonance of the grating produces this type of decrease in the index for TE waves and not for TM waves.

Figure S6D shows the difference in phase delay between TM and TE polarized light. This phase difference controls the strength of the birefringence of the waveplate. The Si nanobeam waveplates have the fast axes perpendicular to the nanobeams. At sufficiently long wavelengths, the nanobeams display a non-resonant behavior and this is the traditional operating regime where the observed birefringence is quite low. Here the phase delay predicted by the full-field simulations and zeroth-order effective medium theory converge. The plot also shows how the resonance for TE illumination gives rise to a substantial phase delay between TE and TM light on the short wavelength side of the TE resonance. It is worth noting that a large phase pickup does not rely on energy storage (and thus loss) inside the absorbing semiconductor nanobeams. The large phase delay is in fact obtained above and away from the TE resonance and thus in a spectral region where the materials absorption is not enhanced by a resonance. In this regard, it is important to realize that the group delay is linked to energy storage and not the phase delay (*28*). The energy storage in the beams near the resonance is fundamentally linked to the rapid change in the phase delay with increasing frequency (*29*, *30*). The large phase delay that results at the short wavelength-side of the resonance is at the origin of the very strong birefringence of the nanobeam waveplates.

S6. Experimental setup for measuring far-field diffraction patterns of DGMOE gratings

A schematic of the experimental setup for measuring the far-field diffraction patterns of the DGMOE grating is illustrated in Fig. S6. The illumination beam is obtained from a white light supercontinuum source (NKT, SuperK Extreme). The polarization state of incident beam is manipulated through a linear polarizer (LP) and a quarter waveplate (QWP). A 20X objective is used to focus the light onto the sample with a spot size of approximately 20 μm. A custom-built imaging system was developed to create real and k-space (i.e. Fourier transformed) images from the grating structures. A flip-mirror controlled the optical path in the setup. With the flip-mirror in place, a magnified real-space image of the sample could be taken by directing the light to a CCD camera. This imaging mode enabled accurate alignment of the incident light with the DGMOE, which itself is mounted on an XYZ translation stage. With the flip-mirror down, a k-space image could be created with the help of a Bertrand lens in a 2-f configuration. In this imaging mode, the diffraction patterns created by the gratings could be captured by a high resolution CCD camera (Princeton Instruments, PIXIS 1024B). A circular polarizer that consists of a quarter waveplate and a linear polarizer was added in place when characterizing the polarization state of the diffracted beams.

S7. Polarization state of the diffracted beams generated by a DGMOE

The diffraction patterns of the nanostructured blazed gratings shown in Fig 3B of the main text were analyzed in k-space using the setup depicted in Fig.S6. For an incident RCP beam at λ = 555 nm, the light experienced a geometric phase pickup of -2θ in propagating through the DGMOE and steered to the left when viewed from the source side. For an incident LCP beam, the light steered in the opposite direction. Upon illumination with linearly polarized light, which consists of equal RCP and LCP components, the light was steered in both directions with each direction an opposite helicity. As a result, a change in the polarization state of the incident beam can be used to control the direction of the diffracted beam. This is shown in Movie S1.

The polarization state of the diffracted beams could be determined by adding a circular polarizer that consists of quarter waveplate (QWP2) and a linear polarizer (LP2), to either transmit just the |L> (left-handed circular polarizer) or |R> polarized light (right-handed circular polarizer). The circular polarizer serves as left-handed circular polarizer when the transmission axis of the linear polarizer (LP2) is at a -45° angle (positive angles representing clockwise rotations from the point of view of the source) relative to the fast axis of the quarter-wave plate (QWP2), while it serves as right-handed circular polarizer at a relative angle of +45°. By rotating the transmission axis of linear polarizer (LP2) while fixing quarter waveplate (QWP2), the circular polarizer can be changed from left-handed circular polarizer to right-handed circular polarizer. For an incident LCP beam at λ = 555 nm, by changing the circular polarizer from left-handed circular polarizer to right-handed circular polarizer alternatively, the zero-order LCP and diffracted RCP can be alternatively transmitted and displayed in diffraction pattern, which was shown in Movie S2.

S8. Intuitive understanding of the Pancharatnam-Berry phase

Pancharatnam-Berry Optical Elements (PBOEs) consist of waveplate elements with space-variant fast axes. The geometric Pancharatnam-Berry (PB) phase is achieved by space-variant polarization manipulations of the waveplate elements. The effectiveness of using Pancharatnam-Berry phase concepts in the design of DGMOEs implies that the nanowire waveplates maintain their desired birefringent behavior, even in the limit where the waveplates are small and consist of just a few truncated nanobeams. This is reasonable as the nanobeams serve leaky resonators supporting highly localized resonances that are primarily controlled by the intrinsic beam properties (material and geometry).

The relative rotation angle θ of the optical axis of a waveplate at a certain location (x,y) will result in a local, geometric phase pickup equal to $\varphi_g(x,y) = 2\theta(x,y)$ for incident LCP light, while the reversed phase is produced for the opposite helicity of incident light (i.e. $\varphi_g = -2\theta$). For an arbitrary incident plane wave $|E_{in}>$ propagating through a PBOE, the transmitted light comprises of three polarization orders (*17*),

$$\left|E_{out}\right\rangle = \sqrt{\eta_E}\left|E_{in}\right\rangle + \sqrt{\eta_R}e^{i2\theta(x,y)}\left|R\right\rangle + \sqrt{\eta_L}e^{-i2\theta(x,y)}\left|L\right\rangle \qquad \text{(Eq. S3)}$$

Here, $\left|R\right\rangle$ and $\left|L\right\rangle$ denote the right- and left-handed circularly polarized unit vectors, respectively. The quantities $\eta_E = |\frac{1}{2}(t_x + t_y e^{i\phi})|^2$, $\eta_R = |\frac{1}{2}(t_x - t_y e^{i\phi})\langle L \mid E_{in}\rangle|^2$, and $\eta_L = |\frac{1}{2}(t_x - t_y e^{i\phi})\langle R \mid E_{in}\rangle|^2$ provide the magnitude of the coupling efficiencies to the different polarization orders. For convenience, we use Dirac Bra-Ket our notation, where $\langle \alpha \mid \beta \rangle$ denotes an inner-product. The function $\theta(x,y)$ describes the spatially-variant distribution of the fast axes of the waveplates. Here, t_x, t_y are the transmission coefficients for light polarized parallel and perpendicular to the fast optical axis, and ϕ is the phase retardation between these linear polarization states. From Eq.S3 it is clear that the optical materials and geometrical properties of the beams, their orientation distribution, and the incident polarization state can be used to control the diffraction properties of the array.

The magnitudes of t_x, t_y, and ϕ determine the distribution of energy into the different polarization orders and are controlled by the optical materials and geometrical properties of the nanobeam waveplate. To realize useful optical elements, it is desired to minimize the amount of light in the $\left|E_{in}\right\rangle$ polarization order that does not experience a geometric phase and thus offers no control over the phase front. For a half wave plate with equal transmission magnitudes ($t_x = t_y$) and a π phase delay, an incident LCP or RCP beam will be 100% transformed to a beam with an opposite-handedness and pick up a geometric phase equal to $\pm 2\theta(x,y)$. The + and – take care of the fact that RCP and LCP light waves experience complementary geometric profiles (*9*). In this ideal case where all of the light emerging from a waveplate picks up a geometric phase, optical elements with unity diffraction efficiency can be created. For our presented nanobeam waveplates a π phase retardation is achieved at a wavelength of 550 nm. The operation of DGMOEs for this condition can also be explained using simple, intuitive graphics (See Supporting info section S8). The grating orientation distribution $\theta(x,y)$ controls the local geometric phase and thus the exact phase profile seen by an incident light wave. Finally, the incident polarization state controls the relative intensities in the right $\left|R\right\rangle$ and left $\left|L\right\rangle$ polarization orders and thus the sign of the geometric phase pickup.

The PB phase can be explained and visualized using a Poincare sphere (*30*). Here, we provide an intuitive description to help understand how geometric rotations of waveplate element introduce a geometric PB phase. Using Fig. S7, we analyze what happens when a waveplate element with a phase retardation of π (i.e. a half-wave plate) is illuminated with an incident of LCP beam. Such an incident beam can be described by a polarization vector with equal amplitudes in the x (green) and y (blue) directions and phase delay of π/2. The half waveplate works by shifting the phase between of the two perpendicular polarizations by π. The net result of this action is to flip the electric field directed along the slow axis and to maintain the electric field along the fast axis. This action can also be viewed as one in which the original polarization vector is flipped to its mirror image with the fast axis serving as the mirror. When considering a helical incident state in which a polarization vector that rotates in time, one can see that the action of the waveplate is to switch helicity from LCP to RCP or vice versa. Fig. S7 (a-h) provide examples of the action of a half-waveplate can have on an incident LCP beam. Fig. S7 panel (a) shows the case where the electric field of an incident |LCP> beam is directed upward (blue vector) at a certain time $t = t_0$. A quarter of an optical cycle later, the light will be directed along the negative x-direction (green vector). The action of the waveplate is to mirror both the blue and green vectors in a mirror placed in the plane of the fast axis and the propagation direction of the light. The action of this mirror is to flip the green vector to the positive x-direction and keep the blue vector in the original direction. As a result, the |LCP> beam is transformed into a |RCP> beam. The other panels show how the mirror action on a |LCP> beam changes when the fast axes of the waveplates are rotated by an angle θ. Independent of the rotation angle, a |RCP> output beam is produced. However, the produced phase delay with respect to panel (a) is given by $\varphi_g = 2\theta$. For example, when $\theta = \pi/2$ (as shown in panel e) the action of the waveplate it to keep the green vector in the same direction and to flip the blue vector from the negative y-direction into the positive y-direction. This produces a |RCP> beam that is delayed by $\varphi_g = 2\theta = \pi$ for incident light of LCP. As such, it will take half an optical cycle longer before the state shown in panel (a) is reached.

A 3D time evolution of wave-vectors plotted in Fig. S7 is shown in Movie S3. The animations of the incident LCP beam (green) and the transmitted RCP beam (red) through metasurface are plotted at the bottom and top respectively in Movie S3. The fast axes of eight half-waveplate elements are indicated as blue lines located in the plane of the waveplate (See Movie S3), and the orientation angles of the fast axes of the half-waveplate elements are in one-to-one correspondence to the ones plotted in Fig. S7.

As shown in Movie S3, the incident LCP wave fronts are nicely aligned (the envelope of wavefronts is indicated by the green, dashed line). After passing through the eight half-waveplate elements that are equally spaced and feature a constant orientation-angle difference $\Delta\theta = \pi/8$ between neighbors, the transmitted RCP waves display a constant phase difference $\Delta\varphi_g = \pi/4$ between neighboring waveplates. Therefore, the wavefronts of the transmitted RCP wave is titled as indicated by red, dashed line shown in Movie S3. By using eight waveplate elements with fast-axes orientation varying between 0 and π, phase pickups can be achieved that covers the full 0-2π range while maintaining equal transmission amplitude~~s~~ for the entire optical component.

S9. Phase profile of DGMOEs serving as lenses and axicons

The geometric pattern of DGMOE axicon consists of series of evenly-spaced, concentric rings. Within each ring the nanobeam antennas are oriented in the same direction. There are 8 discrete levels of rotation angles for the nanobeam antennas, corresponding to 8 discrete levels of geometric phase pickup of 2π for the transmitted light, as shown in Fig. S8A and B. By controlling the local orientation of nanobeam antennas, one can generate the DGMOE axicon shown in Figure 1D of the main text, which has diameter of 64 μm and base angle $\beta = \lambda/3.2\mu m$.

The phase profile for the DGMOE lens shown in Fig. 4A of the main text is presented in Fig. S9. It shows an approximation of a hyperboloidal phase profile of conventional lens with 8 discrete phase levels. In general, to realize a lens with a focal length *f*, the phase profile at any radial location *r* needs to satisfy the relation below:

$$\varphi(r) = 40\pi + \frac{2\pi}{\lambda}(f - \sqrt{r^2 + f^2}) \qquad \text{(Eq. S4)}$$

At wavelength of 550nm, the fabricated lens shown in Fig. 4A has a focal length of 100 μm and a diameter of 96 μm. Consequently, at this wavelength the DGMOE lens has a Numerical Aperture (NA) of 0.43.

S10. Broadband Spectral Properties of the DGMOEs

DGMOEs operate over a broad wavelength range. When the incident wavelength is changed, the metasurface will pick up the same value of phase $\pm 2\theta$ at each location because the phase pickup is solely dependent on the orientation of fast axis θ, therefore the phase profile will remain the same for each wavelength. However, the diffraction efficiency is wavelength-dependent, which varies across the spectrum, depending on the phase retardation and transmission coefficient of the waveplate element at each wavelength.

Fig. 1 in the main text showed that the generated Bessel beam profile by the DGMOE axicon at an illumination wavelength of 550 nm. Fig. S10 show the generated Bessel beam at an alternative wavelength of 700 nm. Compared to the Bessel beam measured at wavelength of 550 nm, it shows a smaller depth of focus at longer wavelength as expected.

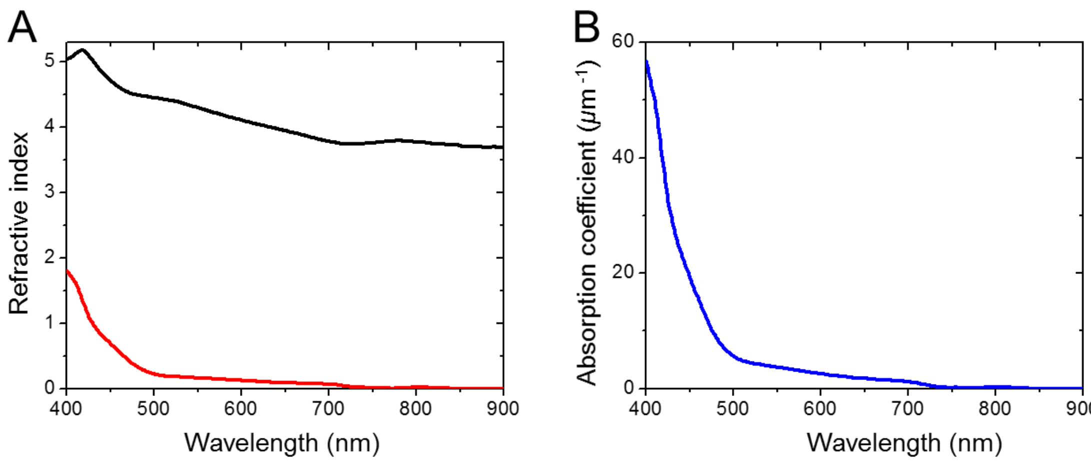

Fig. S1. Optical properties of the poly-silicon (poly-Si) films making up the DGMOEs. (A) The experimentally measured components of the complex refractive index of the deposited poly-Si films. Both the real part (black) and imaginary part (red) are shown. (B) The absorption coefficient of bulk poly-Si as calculated from the complex refractive index.

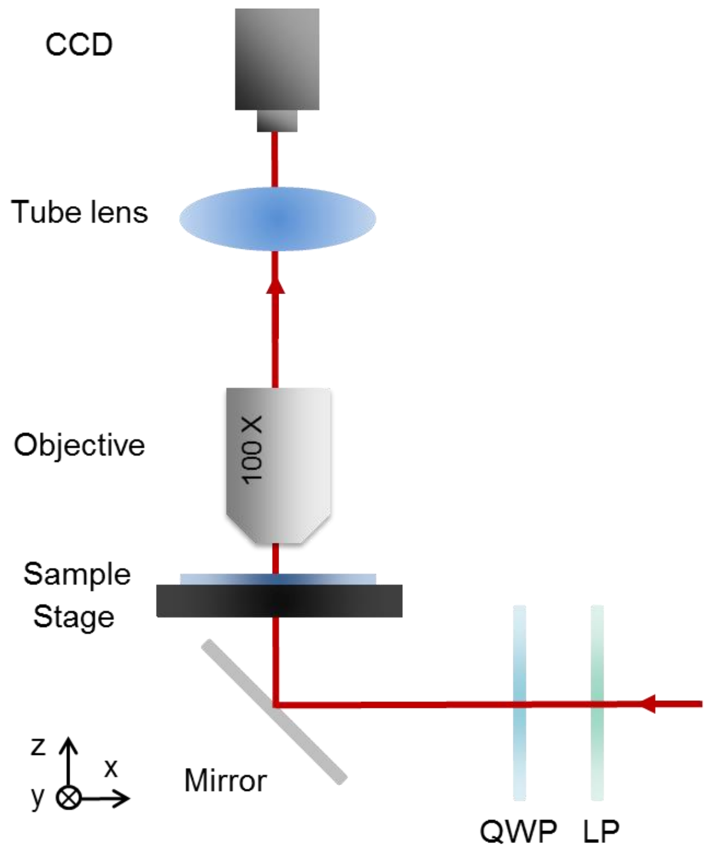

Fig. S2. Experimental Setup for measuring the transmitted light intensity profile of the DGMOEs presented in the main text. Abbreviations used for the optical components are: CCD for Charge Coupled Device or CCD camera, QWP for quarter waveplate, and LP for linear polarizer.

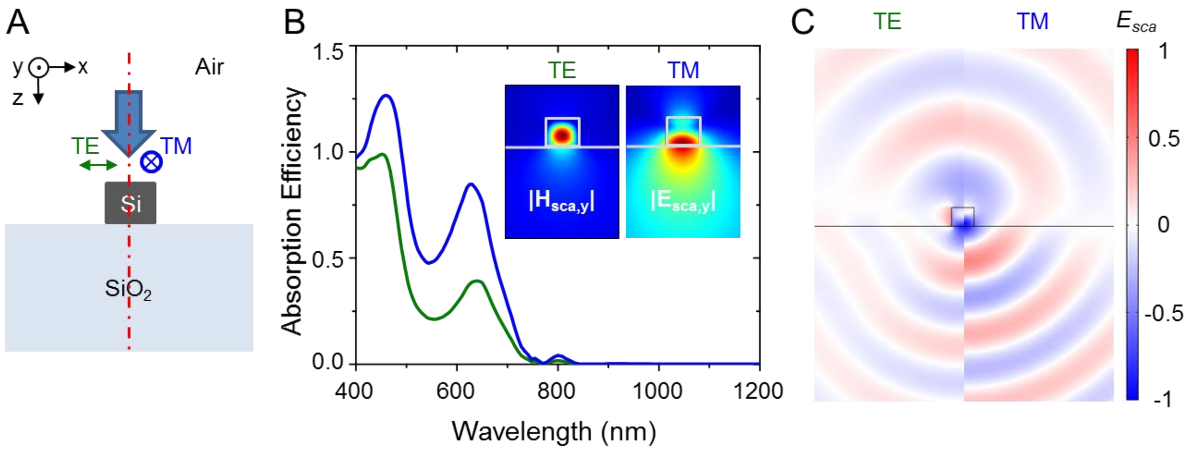

Fig. S3. Phase delay in the light scattering of TE and TM polarized light by an individual Si nanobeam. (A) Schematic view of single Si nanobeam placed on a quartz substrate. (B) Simulated absorption efficiency spectra of a single Si nanobeam with a width of 120 nm and thickness of 100 nm, under TE (green) and TM (blue) polarized illumination. Insets show the scattered magnetic field distribution $|H_{sca,y}|$ for TE and the scattered electrical field distribution $|E_{sca,y}|$ of TM illumination at the resonant wavelength of the beam of 630 nm. (C) A full field simulation of the scattered electric field from a single nanowire under TE (left) and TM (right) polarized illumination at wavelength of 550 nm. The field distribution was obtained by means of finite element analysis solving for scattered field and the color plot is normalized to the maximum amplitude. As the beams are brought together in a dense array, both the absorption resonances and the associated phase delays between TE and TM polarized light evolve from those of the individual beams. That said, knowledge of the resonances of the individual beams can help in expediting the design of the array as the basic resonance of the nanobeams can be encoded into/recognized in the resonant optical properties of the nanobeam array.

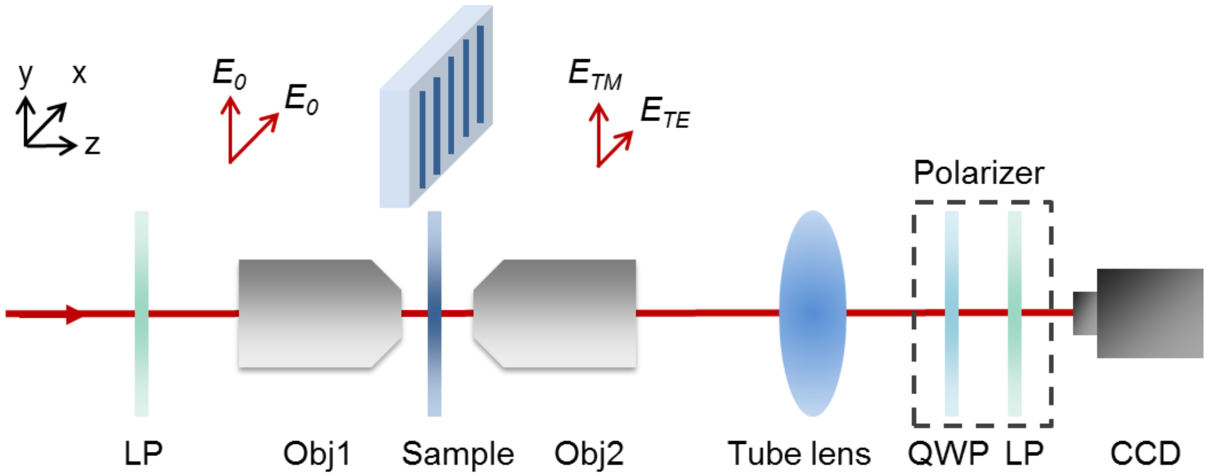

Fig. S4. Experimental Setup for measuring the optical properties of nanowire arrays. Abbreviations for optical components: LP: linear polarizer; QWP: quarter waveplate; Obj1: 20X objective lens for focusing incident beam; Obj2: 20X objective lens for imaging the sample.

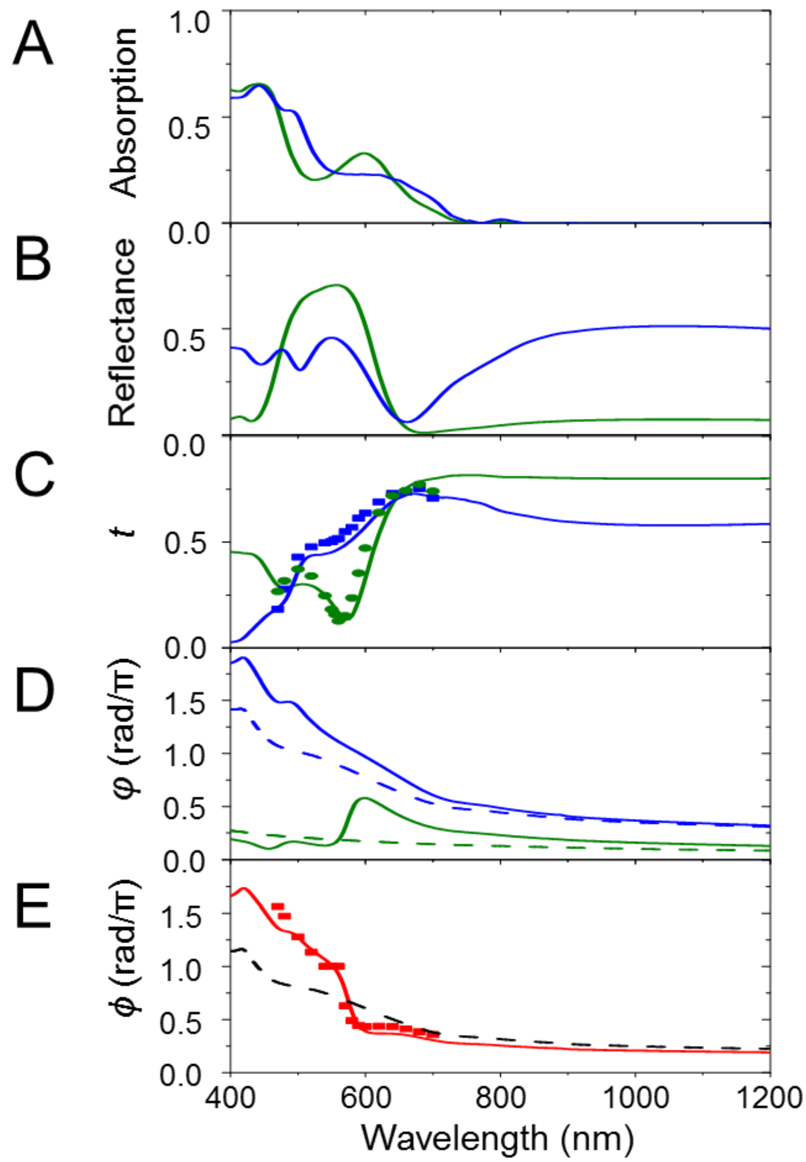

Fig. S5. Optical properties of a fabricated nanobeam-waveplate consisting of 120-nm-wide, 100-nm-thick Si nanobeams spaced by 200 nm. (A) Simulated absorption spectra of the waveplate under TE (green) and TM (blue) polarized illumination. (B) Simulated spectra of reflectance of the waveplate under TE (green) and TM (blue) polarized illumination. (C) Spectra of the transmission coefficient of the fabricated waveplate for TE (green) and TM (blue) polarization. Both simulation (continuous line) and experiment (dotted line) are shown. (D) Simulated spectra of the phase delay of the transmitted light for TE (green) and TM (blue) illumination with respect to a reference case in which the nanobeams are absent. The results from both full-field electromagnetic simulations (continuous line) and an approximate effective medium theory (dashed line) are shown. (E) Spectra of the phase retardation of TM polarized light with respect to TE polarized light. Both full-field electromagnetic simulations (continuous line) and the experiment (dotted line) are shown at different illumination wavelengths. Calculated spectra of the phase retardation based on an effective medium theory (black dashed line) are shown for reference.

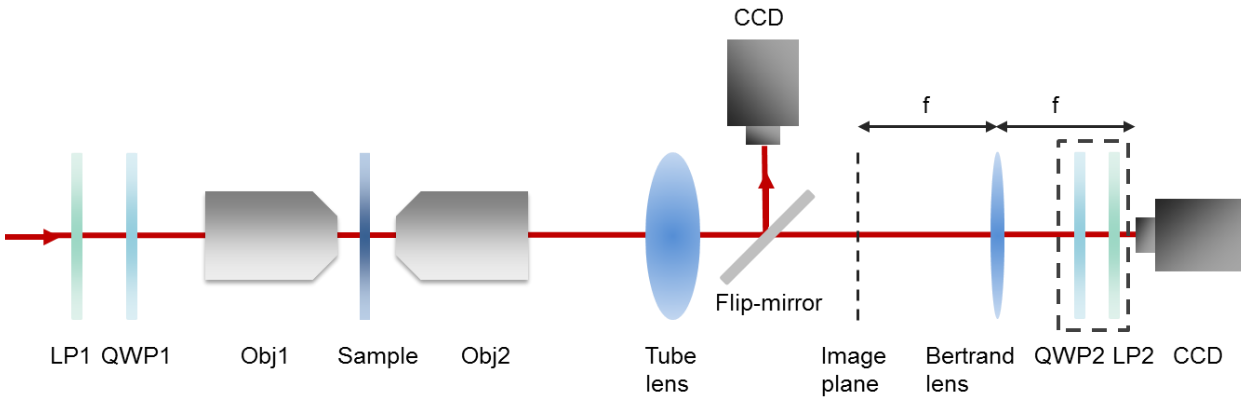

Fig. S6. Experimental setup for measuring the far-field diffraction patterns of the DGMOE serving as a blazed grating. Abbreviations for optical components: LP1: linear polarizer for illumination polarization manipulation; QWP1: quarter waveplate for illumination polarization manipulation; Obj1: a 20X Objective lens used to focus incident beam; Obj2: 20X Objective lens for imaging; QWP2: quarter waveplate for illumination polarization manipulation; LP2: linear polarizer for illumination polarization manipulation.

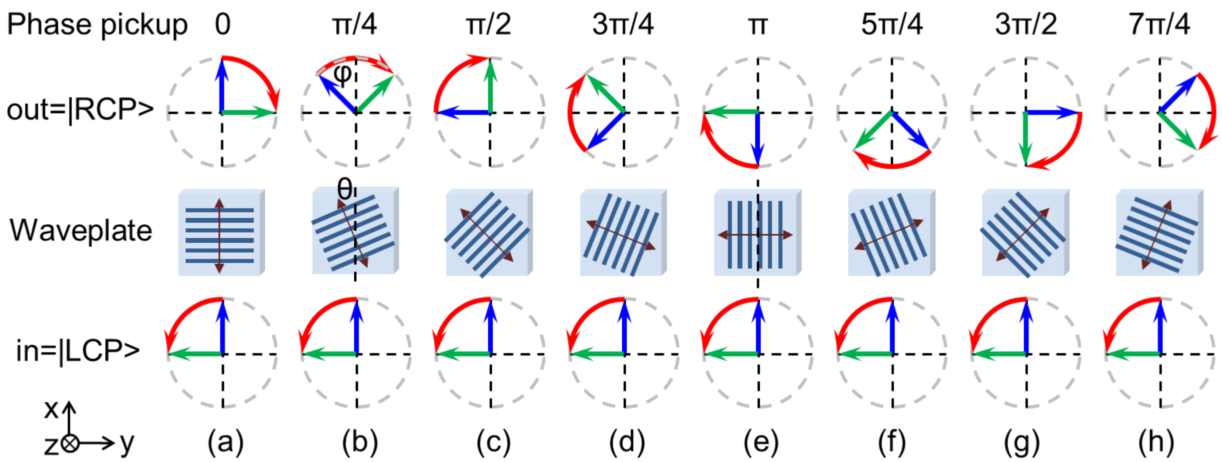

Fig. S7. Pictorial description of the origin for the occurrence of a Pancharatnam-Berry phase for the case of half waveplates. (Bottom row) schematic depicting the rotation of the polarization vector of an incident light beam with left circular polarization, i.e. a |LCP> state. (Middle) half-waveplate elements constructed from nanobeam arrays with their fast axis oriented at different angles θ; (Top) schematic of polarization vectors of the transmitted light behind the waveplate elements. Circular polarizations and anti-clockwise orientation angles of fast axis of waveplate are defined from the point of view of the source.

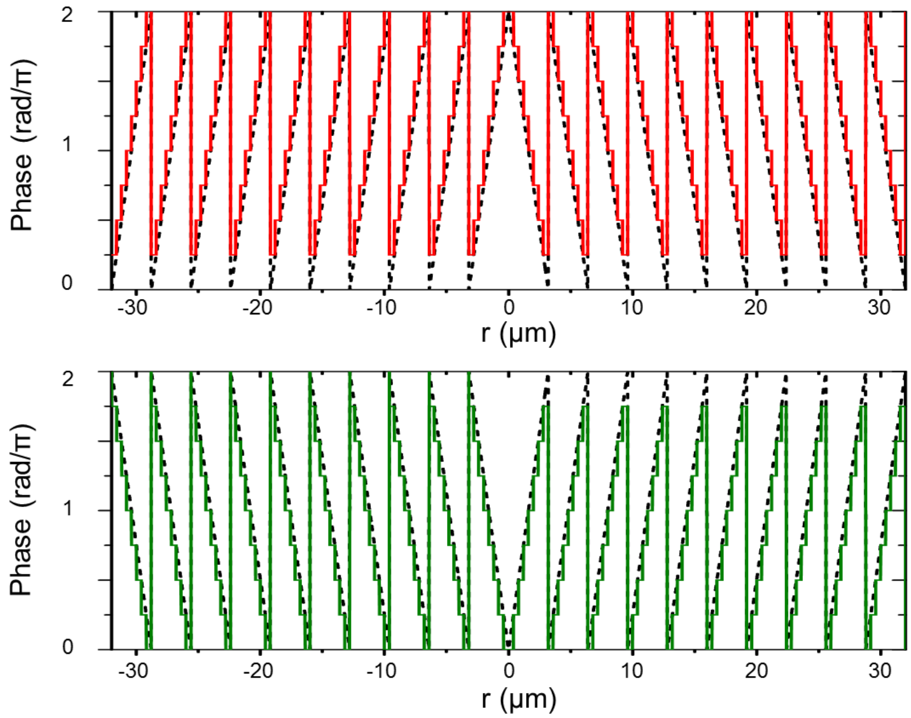

Fig. S8. Phase profile of the DGMOE serving as an axicon. (A) For illumination of the axicon with left circular polarized light, the discretized (red solid line) and continuous (black dashed line) phase profiles of DGMOE axicon are shown. (B) A reversed discretized phase profile (green solid line) and continuous (black dashed line) are seen for illumination with right circular polarized light.

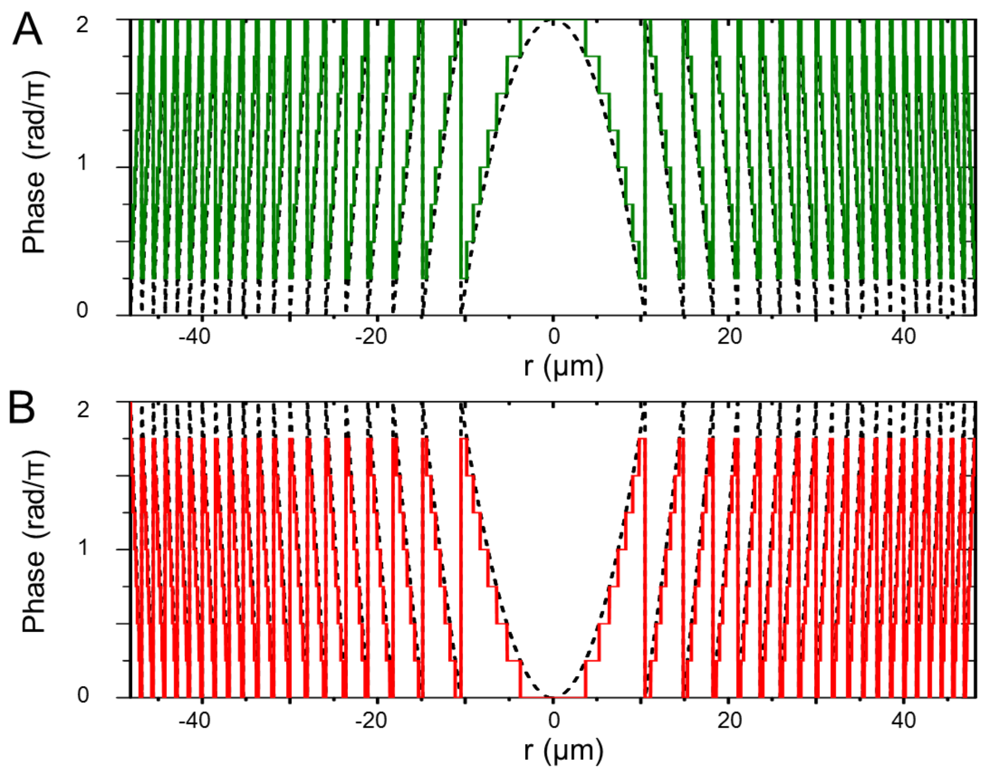

Fig. S9. Phase profile of DGMOE lens. (A) For illumination with RCP light, the discretized (green solid line) and continuous (black dashed line) show the phase profile of a DGMOE lens. (B) The reversed profile to A shown by the red solid line and continuous black dashed line represent the phase profile appropriate for illumination with LCP light.

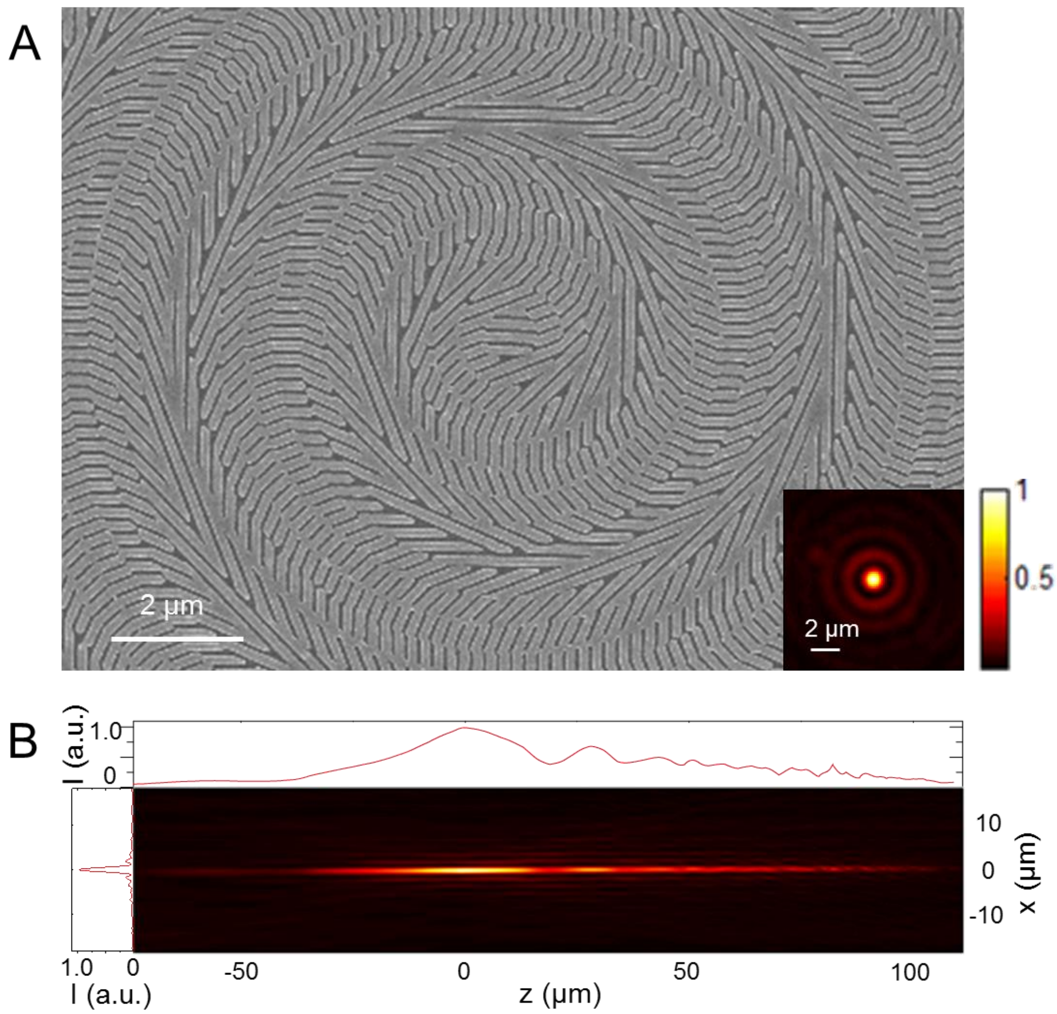

Fig. S10. Generated Bessel beam by a DGMOE of axicon at an illumination wavelength of 700 nm. (A) SEM image of the fabricated DGMOE axicon. The inset shows the transversal distribution of the Bessel beam generated by the DGMOE of axicon at a wavelength of 700 nm. (B) Measured intensity profile of the non-diffracting Bessel beam generated behind the axicon in the x-z plane. The intensity profile measured along the center of Bessel beam is plotted in the inset along the optical axis and shows a smaller depth of focus than achieved at 550 nm (Fig. 1E of the main text).

Movie S1

Light steering with a DGMOE blazed grating. Diffraction pattern obtained from the grating shown in Fig. 3B of the main text upon illumination with 555 nm wavelength light. This supplementary video (Movie S1) shows the changes in the diffraction pattern upon changing the polarization state of the incidence beam successively from RCP - linear - LCP - linear - RCP, by manually rotating the fast axis of quarter waveplate QWP1 depicted in Fig. S6. over 360°, while fixing the transmission axis of linear polarizer (LP1 as noted in Fig. S6).

Movie S2

Measurement of the polarization state of the diffracted beams. Diffraction patterns obtained with an incident LCP beam at a wavelength light 555 nm. The circular polarizer that consists of a quarter waveplate (QWP2) and a linear polarizer (LP2) was added to characterize the polarization state of the diffracted beams. The fast axis of QWP2 is aligned with vertical axis, while the transmission axis of LP2 is manually rotated to alternatively transmit LCP and RCP beam. Movie S2 shows the changes in the diffraction pattern upon changing the circular polarizer from left-handed circular polarizer to right-handed circular polarizer alternatively, by manually rotating the transmission axis of linear polarizer (LP2) while fixing quarter waveplate (QWP2).

Movie S3

3D time evolution of wave-vectors of a Pancharatnam-Berry phase for the case of half waveplates as plotted in Fig. S7. (Bottom) the animations of the incident LCP waves (green); (Middle) the fast axes (blue) of eight half-waveplate elements that are equally spaced and have constant angle difference $\Delta\theta = \pi/8$ between neighbors, and their orientation angles are one-to-one correspondence to the ones plotted in Fig. S8; (Top) the animations of the transmitted RCP waves behind the waveplate elements. The envelope of wavefronts of incident waves (green dash line) is flat, since the incident LCP waves are propagating at the same phase. The envelope of wavefronts of transmitted RCP waves behind the waveplate elements (red dash line) is tilted by λ along propagation z axis, due to the full 0-2π range PB phase pickup by the eight waveplate elements with fast-axes orientation varying between 0 and π.

References and Notes

1. L. Verslegers, P. B. Catrysse, Z. Yu, J. S. White, E. S. Barnard, M. L. Brongersma, S. Fan, Planar lenses based on nanoscale slit arrays in a metallic film. *Nano Lett.* **9**, 235–238 (2009). Medline doi:10.1021/nl802830y

2. D. Fattal, J. Li, Z. Peng, M. Fiorentino, R. G. Beausoleil, Flat dielectric grating reflectors with focusing abilities. *Nat. Photonics* **4**, 466–470 (2010). doi:10.1038/nphoton.2010.116

3. C. J. Chang-Hasnain, High-contrast gratings as a new platform for integrated optoelectronics. *Semicond. Sci. Technol.* **26**, 014043 (2011). doi:10.1088/0268-1242/26/1/014043

4. F. Afshinmanesh, J. S. White, W. Cai, M. L. Brongersma, Measurement of the polarization state of light using an integrated plasmonic polarimeter. *Nanophotonics* **1**, 125–129 (2012). doi:10.1515/nanoph-2012-0004

5. E. T. F. Rogers, J. Lindberg, T. Roy, S. Savo, J. E. Chad, M. R. Dennis, N. I. Zheludev, A super-oscillatory lens optical microscope for subwavelength imaging. *Nat. Mater.* **11**, 432–435 (2012). Medline doi:10.1038/nmat3280

6. N. Engheta, Circuits with light at nanoscales: Optical nanocircuits inspired by metamaterials. *Science* **317**, 1698–1702 (2007). Medline doi:10.1126/science.1133268

7. A. V. Kildishev, A. Boltasseva, V. M. Shalaev, Planar photonics with metasurfaces. *Science* **339**, 1232009 (2013). Medline doi:10.1126/science.1232009

8. N. Yu, P. Genevet, M. A. Kats, F. Aieta, J. P. Tetienne, F. Capasso, Z. Gaburro, Light propagation with phase discontinuities: Generalized laws of reflection and refraction. *Science* **334**, 333–337 (2011). Medline doi:10.1126/science.1210713

9. X. Ni, N. K. Emani, A. V. Kildishev, A. Boltasseva, V. M. Shalaev, Broadband light bending with plasmonic nanoantennas. *Science* **335**, 427 (2012). Medline doi:10.1126/science.1214686

10. P. Spinelli, M. A. Verschuuren, A. Polman, Broadband omnidirectional antireflection coating based on subwavelength surface Mie resonators. *Nat. Commun.* **3**, 692 (2012). Medline doi:10.1038/ncomms1691

11. L. Cao, P. Fan, A. P. Vasudev, J. S. White, Z. Yu, W. Cai, J. A. Schuller, S. Fan, M. L. Brongersma, Semiconductor nanowire optical antenna solar absorbers. *Nano Lett.* **10**, 439–445 (2010). Medline doi:10.1021/nl9036627

12. L. Cao, P. Fan, E. S. Barnard, A. M. Brown, M. L. Brongersma, Tuning the color of silicon nanostructures. *Nano Lett.* **10**, 2649–2654 (2010). Medline doi:10.1021/nl1013794

13. Y. Yang, W. Wang, P. Moitra, I. I. Kravchenko, D. P. Briggs, J. Valentine, Dielectric meta-reflectarray for broadband linear polarization conversion and optical vortex generation. *Nano Lett.* **14**, 1394–1399 (2014). Medline doi:10.1021/nl4044482

14. C. Wu, N. Arju, G. Kelp, J. A. Fan, J. Dominguez, E. Gonzales, E. Tutuc, I. Brener, G. Shvets, Silicon-based infrared metamaterials with ultra-sharp Fano resonances. http://arxiv.org/abs/1309.6616 (2013).

15. A. Pors, O. Albrektsen, I. P. Radko, S. I. Bozhevolnyi, Gap plasmon-based metasurfaces for total control of reflected light. *Sci. Rep.* **3**, 2155 (2013). Medline doi:10.1038/srep02155

16. S. Sun, K. Y. Yang, C. M. Wang, T. K. Juan, W. T. Chen, C. Y. Liao, Q. He, S. Xiao, W. T. Kung, G. Y. Guo, L. Zhou, D. P. Tsai, High-efficiency broadband anomalous reflection by gradient meta-surfaces. *Nano Lett.* **12**, 6223–6229 (2012). Medline doi:10.1021/nl3032668

17. R. K. Mongia, A. Ittipiboon, *IEEE Trans. Antenn. Propag.* **45**, 1348–1356 (1997). doi:10.1109/8.623123

18. L. Cao, J. S. White, J. S. Park, J. A. Schuller, B. M. Clemens, M. L. Brongersma, Engineering light absorption in semiconductor nanowire devices. *Nat. Mater.* **8**, 643–647 (2009). Medline doi:10.1038/nmat2477

19. Z. Bomzon, G. Biener, V. Kleiner, E. Hasman, Radially and azimuthally polarized beams generated by space-variant dielectric subwavelength gratings. *Opt. Lett.* **27**, 285–287 (2002). Medline doi:10.1364/OL.27.000285

20. A. Niv, G. Biener, V. Kleiner, E. Hasman, Propagation-invariant vectorial Bessel beams obtained by use of quantized Pancharatnam-Berry phase optical elements. *Opt. Lett.* **29**, 238–240 (2004). Medline doi:10.1364/OL.29.000238

21. Materials and methods are available as supplementary materials on *Science* Online.

22. S. Pancharatnam, *Proc. Indiana Acad. Sci.* **A44**, 247–262 (1956).

23. M. V. Berry, The adiabatic phase and Pancharatnam's phase for polarized light. *J. Mod. Opt.* **34**, 1401–1407 (1987). doi:10.1080/09500348714551321

24. Z. Bomzon, G. Biener, V. Kleiner, E. Hasman, Space-variant Pancharatnam-Berry phase optical elements with computer-generated subwavelength gratings. *Opt. Lett.* **27**, 1141–1143 (2002). Medline doi:10.1364/OL.27.001141

25. A. Niv, G. Biener, V. Kleiner, E. Hasman, Spiral phase elements obtained by use of discrete space-variant subwavelength gratings. *Opt. Commun.* **251**, 306–314 (2005). doi:10.1016/j.optcom.2005.03.002

26. E. Hasman, V. Kleiner, G. Biener, A. Niv, Polarization dependent focusing lens by use of quantized Pancharatnam–Berry phase diffractive optics. *Appl. Phys. Lett.* **82**, 328–330 (2003). doi:10.1063/1.1539300

27. D. J. Bergman, The dielectric constant of a composite material—A problem in classical physics. *Phys. Rep.* **43**, 377–407 (1978). doi:10.1016/0370-1573(78)90009-1

28. M. Gerken, D. A. B. Miller, Relationship between the superprism effect in one-dimensional photonic crystals and spatial dispersion in nonperiodic thin-film stacks. *Opt. Lett.* **30**, 2475–2477 (2005). Medline doi:10.1364/OL.30.002475

29. K. D. Li, W. H. Knox, N. M. Pearson, Broadband cubic-phase compensation with resonant Gires-Tournois interferometers. *Opt. Lett.* **14**, 450–452 (1989). Medline doi:10.1364/OL.14.000450

30. O. Schwelb, Transmission, group delay, and dispersion in single-ring optical resonators and add/drop filters—A tutorial overview. *J. Lightwave Technol.* **22**, 1380–1394 (2004). doi:10.1109/JLT.2004.827666